



An evaluation of the MPM for simulating dynamic failure with damage diffusion

Z. Chen ^{a,*}, W. Hu ^a, L. Shen ^a, X. Xin ^a, R. Brannon ^b

^a *Department of Civil and Environmental Engineering, University of Missouri, E2509 Engineering Bldg. East, Columbia, MO 65211-2200, USA*

^b *Department of Physics and Simulation Frameworks, Sandia National Laboratories, Albuquerque, NM 87185-0820, USA*

Received 22 March 2002; accepted 16 April 2002

Abstract

For dynamic brittle failure, conventional mesh-based methods, such as the finite element method and finite difference method, are handicapped when localized large deformations and subsequent transitions from continuous to discontinuous failure modes occur. To evaluate the potential of the material point method (MPM) in simulating dynamic brittle failure involving different failure modes, the essential features of the MPM are explored for wave and impact problems, and combined wave and diffusion problems are then solved by using the MPM. Through the comparison with the experimental, analytical and numerical data available, it appears that the MPM is a robust tool to simulate multi-physics problems such as dynamic failure under impact.

© 2002 Published by Elsevier Science Ltd.

Keywords: Dynamic failure; Diffusion; Impact; Localization; Meshless

1. Introduction

Recently, several kinds of “meshless” methods for spatial discretization have been proposed in the computational mechanics community. Since these meshless methods do not use a rigid mesh connectivity as compared with the conventional mesh-based methods such as the finite element method (FEM) and the finite difference method (FDM), they have been applied to some complex problems of current interests such as impact/contact, localization, crack propagation, penetration, perforation and fragmentation. Although academic exercises have demonstrated the robustness and potential of these meshless methods, they have not found their way successfully into general practical applications due to some unsolved problems such as boundary treatments, large rotation, and interactions among different material phases. Especially, these methods have not been validated and verified in a systematic way, based on the analytical, numerical and experimental data available.

* Corresponding author. Tel.: +1-573-882-0311; fax: +1-573-882-4784.

E-mail address: chenzh@missouri.edu (Z. Chen).

As one of the innovative spatial discretization methods, the material point method (MPM) is an extension to solid mechanics problems of a hydrodynamics code called FLIP which, in turn, evolved from the particle-in-cell method dating back to the pioneering work of Harlow [1]. The motivation for the development of MPM was to simulate problems such as impact/contact, penetration and perforation with history-dependent internal state variables without invoking any master/slave relationship, as shown in the early publications about the MPM [2–4]. The essential idea is to take advantage of both the Eulerian and Lagrangian methods. To evaluate the potential of the MPM in simulating multi-physics problems, such as dynamic brittle failure, the essential features of the MPM are explored for wave and impact problems, and combined wave and diffusion problems are then solved by using the MPM. Through the comparison with the available analytical solutions, numerical solutions via the FEM, and experimental data on failure waves, we demonstrate that the MPM could become a robust spatial discretization tool to simulate dynamic brittle failure in general.

2. Essential features of the material point method

For a continuum body under purely mechanical loading, the governing differential equations can be derived from the conservation equation for mass,

$$\frac{d\rho}{dt} + \rho \nabla \cdot \mathbf{v} = 0 \quad (1)$$

and the conservation equation for momentum,

$$\rho \mathbf{a} = \nabla \cdot \mathbf{s} + \rho \mathbf{b} \quad (2)$$

supplemented with a suitable constitutive equation, and kinematic relation between strain and displacement. In Eqs. (1) and (2), $\rho(\mathbf{x}, t)$ is the mass density, $\mathbf{v}(\mathbf{x}, t)$ is the velocity, $\mathbf{a}(\mathbf{x}, t)$ is the acceleration, $\mathbf{s}(\mathbf{x}, t)$ is the Cauchy stress tensor, $\mathbf{b}(\mathbf{x}, t)$ is the specific body force, and the dot represents the inner product between tensor quantities of the first or higher orders. The vector \mathbf{x} is the current position at time t of any material point in the continuum. For given boundary and initial data, the governing differential equations can be solved either analytically or numerically, if they are well posed. The key difference among different spatial discretization methods is the way in which the gradient and divergence terms are calculated.

The MPM discretizes a continuum body with the use of a finite set of N_p material points in the original configuration that are tracked throughout the deformation process. Let \mathbf{x}_p^t ($p = 1, 2, \dots, N_p$) denote the current position of material point p at time t . Each material point at time t has an associated mass M_p , density ρ_p^t , velocity \mathbf{v}_p^t , Cauchy stress tensor \mathbf{s}_p^t , strain \mathbf{e}_p^t , and any other internal state variables necessary for the constitutive model. Thus, these material points provide a Lagrangian description of the continuum body. Since each material point contains a fixed amount of mass for all time, Eq. (1) is automatically satisfied. At each time step, information from the material points is mapped to a background computational mesh (grid). This mesh covers the computational domain of interest, and is chosen for computational convenience. After the information is mapped from the material points to the mesh nodes, the discrete formulation of Eq. (2) can be obtained on the mesh nodes, as described below.

The weak form of Eq. (2) can be found, based on the standard procedure used in the FEM [2–4], to be

$$\int_{\Omega} \rho \mathbf{w} \cdot \mathbf{a} d\Omega = - \int_{\Omega} \rho \mathbf{s}^s : \nabla \mathbf{w} d\Omega + \int_{S^c} \rho \mathbf{c}^s \cdot \mathbf{w} dS + \int_{\Omega} \rho \mathbf{w} \cdot \mathbf{b} d\Omega \quad (3)$$

in which \mathbf{w} denotes the test function, \mathbf{s}^s is the specific stress (i.e., stress divided by mass density, $\mathbf{s}^s = \mathbf{s}/\rho$), Ω is the current configuration of the continuum, S^c is that part of the boundary with a prescribed traction, and \mathbf{w} is assumed to be zero on the boundary with a prescribed displacement. To prescribe nonzero tractions on

a boundary, the concept of a boundary layer can be introduced here to enforce the traction boundary condition, with the use of the specific traction vector \mathbf{c}^s (i.e., traction divided by mass density). Because of this boundary treatment, a moving boundary or material interface can be easily traced in the MPM.

Since the whole continuum body is described with the use of a finite set of material points (mass elements), the mass density can be written as

$$\rho(\mathbf{x}, t) = \sum_{p=1}^{N_p} M_p \delta(\mathbf{x} - \mathbf{x}_p^t) \quad (4)$$

where δ is the Dirac delta function with dimension of the inverse of volume. Substitution of Eq. (4) into Eq. (3) converts the integrals to the sums of quantities evaluated at the material points, namely

$$\sum_{p=1}^{N_p} M_p [\mathbf{w}(\mathbf{x}_p^t, t) \cdot \mathbf{a}(\mathbf{x}_p^t, t)] = \sum_{p=1}^{N_p} M_p \left[-s^s(\mathbf{x}_p^t, t) : \nabla \mathbf{w}|_{\mathbf{x}_p^t} + \mathbf{w}(\mathbf{x}_p^t, t) \cdot \mathbf{c}^s(\mathbf{x}_p^t, t) h^{-1} + \mathbf{w}(\mathbf{x}_p^t, t) \cdot \mathbf{b}(\mathbf{x}_p^t, t) \right] \quad (5)$$

in which h represents the thickness of a boundary layer that we introduce as an approximate means of enforcing boundary conditions. As can be seen from Eq. (5), interactions among different material points are reflected only through the gradient terms, and a suitable set of material points must be chosen to represent the boundary layer. In the MPM, a background computational mesh is required to calculate the gradient terms. To do so, suppose that a computational mesh is constructed of 2-node cells for one-dimensional problems, 4-node cells for two-dimensional problems, and 8-node cells for three-dimensional problems, respectively. These cells are then employed to define standard nodal basis functions, $N_i(\mathbf{x})$, associated with spatial nodes $\mathbf{x}_i(t)$, $i = 1, 2, \dots, N_n$, with N_n being the total number of mesh nodes. The nodal basis functions are assembled from conventional finite element shape functions. For instance, the shape functions for a 2-node cell take the forms of

$$N_1 = 1 - \xi \quad (6a)$$

$$N_2 = \xi \quad (6b)$$

where ξ is the natural coordinate of a material point in the cell along the x -direction. For two-dimensional problems, a 4-node cell is employed with the shape functions given by

$$N_1 = (1 - \xi)(1 - \eta) \quad (7a)$$

$$N_2 = \xi(1 - \eta) \quad (7b)$$

$$N_3 = \xi\eta \quad (7c)$$

$$N_4 = (1 - \xi)\eta \quad (7d)$$

in which ξ and η are the natural coordinates of a material point in the cell along the x - and y -direction, respectively. The coordinates of any material point in a cell can then be represented by

$$\mathbf{x}_p^t = \sum_{i=1}^{N_n} \mathbf{x}_i^t N_i(\mathbf{x}_p^t) \quad (8)$$

If the displacements of any material point in a cell are defined by the nodal displacements, $\mathbf{u}_i^t(t)$, it follows that

$$\mathbf{u}_p^t = \sum_{i=1}^{N_n} \mathbf{u}_i^t N_i(\mathbf{x}_p^t) \quad (9)$$

Since the same basis functions are used for both spatial coordinates and displacements, kinematic compatibility demands that the basis functions must advect with the material, as in an updated Lagrangian framework. In other words, the material time rates of the basis functions must be zero. Hence, it follows that the velocity and acceleration of any material point in a cell are represented by

$$\mathbf{v}_p^t = \sum_{i=1}^{N_n} \mathbf{v}_i^t N_i(\mathbf{x}_p^t) \quad (10)$$

and

$$\mathbf{a}_p^t = \sum_{i=1}^{N_n} \mathbf{a}_i^t N_i(\mathbf{x}_p^t) \quad (11)$$

with \mathbf{v}_i^t and \mathbf{a}_i^t being nodal velocities and accelerations, respectively. The test function also has a similar form,

$$\mathbf{w}_p^t = \sum_{i=1}^{N_n} \mathbf{w}_i^t N_i(\mathbf{x}_p^t) \quad (12)$$

The use of Eqs. (8)–(12) ensures that the associated vectors are continuous across the cell boundary. However, the gradients of these vectors are not continuous across the cell boundary due to the use of linear shape functions. Note that the variables evaluated at material points are related to the nodal values through the shape functions, as can be seen from Eqs. (8)–(12).

Substituting Eqs. (11) and (12) into Eq. (5) yields

$$\sum_{i=1}^{N_n} \mathbf{w}_i^t \cdot \sum_{j=1}^{N_n} m_{ij}^t \mathbf{a}_j^t = - \sum_{i=1}^{N_n} \mathbf{w}_i^t \cdot \sum_{j=1}^{N_p} M_p \mathbf{s}_p^{s,t} \cdot \nabla N_i|_{\mathbf{x}_p^t} + \sum_{i=1}^{N_n} \mathbf{w}_i^t \cdot \mathbf{c}_i^t + \sum_{i=1}^{N_n} \mathbf{w}_i^t \cdot \mathbf{b}_i^t \quad (13)$$

at time t . In Eq. (13), the consistent mass matrix is given by

$$m_{ij}^t = \sum_{p=1}^{N_p} M_p N_i(\mathbf{x}_p^t) N_j(\mathbf{x}_p^t) \quad (14)$$

with corresponding lumped nodal masses

$$m_i^t = \sum_{p=1}^{N_p} M_p N_i(\mathbf{x}_p^t) \quad (15)$$

The discrete specific traction takes the form of

$$\mathbf{c}_i^t = \sum_{p=1}^{N_p} M_p \mathbf{c}_p^{s,t} h^{-1} N_i(\mathbf{x}_p^t) \quad (16)$$

with $\mathbf{c}_p^{s,t} = \mathbf{c}^s(\mathbf{x}_p^t, t)$, while the specific body force is discretized as

$$\mathbf{b}_i^t = \sum_{p=1}^{N_p} M_p \mathbf{b}_p^t N_i(\mathbf{x}_p^t) \quad (17a)$$

with $\mathbf{b}_p^t = \mathbf{b}(\mathbf{x}_p^t, t)$. Alternatively, if the vector \mathbf{b} is a known function of position and time, as for gravity, then the nodal body force can be computed directly by

$$\mathbf{b}_i^t = \mathbf{b}(\mathbf{x}_p^t, t) m_i^t \quad (17b)$$

Since \mathbf{w}_i^t are arbitrary except where the components of displacement are prescribed, Eq. (13) becomes

$$m_i^t \mathbf{a}_i^t = (\mathbf{f}_i^t)^{\text{int}} + (\mathbf{f}_i^t)^{\text{ext}} \quad (18)$$

for a lumped mass matrix, where the internal force vector is given by

$$(\mathbf{f}_i^t)^{\text{int}} = - \sum_{p=1}^{N_p} M_p \mathbf{s}_p^{s,t} \cdot \mathbf{G}_i(\mathbf{x}_p^t) \quad (19)$$

with $\mathbf{s}_p^{s,t} = \mathbf{s}^s(\mathbf{x}_p^t, t)$ and $\mathbf{G}_i(\mathbf{x}_p^t) = \nabla N_i|_{\mathbf{x}_p^t}$, and the external force vector is

$$(\mathbf{f}_i^t)^{\text{ext}} = \mathbf{c}_i^t + \mathbf{b}_i^t \quad (20)$$

As can be observed from Eqs. (15)–(17a,b) and (19), the information is mapped from material points to the nodes of the cell containing these points, through the use of shape functions. If a material point is located in the center of a cell, the information from the particle would be equally mapped to the cell nodes, as can be found from the shape functions defined in Eqs. (6a,b) and (7a–d).

An explicit time integrator is used to solve Eq. (18) for the nodal accelerations, with the time step satisfying the stability condition, i.e., the critical time step being the smallest ratio of the cell size to the wave speed. For small displacements, the spatial discretization via the MPM is equivalent to that via the FEM using Gauss points at the same locations as those of material points in each cell. Therefore, the convergence behavior of the explicit time integrator used to solve Eq. (18) is similar to that employed to integrate the corresponding equation in the FEM. However, no consistent theoretical results have been obtained for the convergence behaviors of time integrators when large deformations and the transition from continuous to discontinuous failure modes occur. A reasonable time step is usually found through numerical experiments. Based on the framework of the MPM, the boundary conditions are enforced on the cell nodes. After the equations of motion are solved on the cell nodes, the new nodal values of velocity are then used to update the position of the material points. The strain increment for each material point is determined with the use of the gradient of the nodal basis function evaluated at the material point position. The corresponding stress increment can be found from the constitutive model. Any internal state variables can also be assigned to the material points and transported along with them. Once the material points have been completely updated, the computational cycle is complete for this time step. The computational mesh used in the current cycle may be discarded, and a new mesh is defined, if desired, for the next time step, in the spirit of the updated Lagrangian frame.

The key feature of the MPM is the use of the same set of nodal basis functions for both the mapping from material points to cell nodes, and the mapping from cell nodes to material points. As a result, the use of the single-valued mapping functions yields a natural no-slip contact/impact scheme so that no interpenetration would occur for penetration problems.

To simulate shock wave propagation, a viscous damping stress tensor, \mathbf{q}_p^t , can be added to the material point stress tensor, \mathbf{s}_p^t [5]. Based on the work by Wilkins [6], the viscous damping stress takes the form of

$$\mathbf{q}_p^t = \sqrt{c_{\text{max}}^2 g \rho_p^t \lambda D_p^t} \left[c_1 + \frac{c_2 |D_p^t|}{\max |D_p^t|} \right] \mathbf{i} \quad (21)$$

where \mathbf{i} being the second-order identity tensor, and

$$D_p^t = \begin{cases} \nabla \cdot \mathbf{v}|_{\mathbf{x}_p^t} & \nabla \cdot \mathbf{v}|_{\mathbf{x}_p^t} < 0 \\ 0 & \nabla \cdot \mathbf{v}|_{\mathbf{x}_p^t} \geq 0 \end{cases} \quad (22)$$

In Eq. (21), c_{max} is the maximum sound speed, g is a geometric constant proportional to the mesh size, λ is an artificial bulk modulus, and c_1 and c_2 are constants. The variable D_p^t defined in Eq. (22) forces the

viscous damping stress to be zero unless the material point is in compression. Through numerical experiments, the values of c_1 and c_2 could be chosen so that a reasonable shock wavefront can be obtained for given geometry, material properties and loading conditions.

3. Undamped one-dimensional problems

To explore and demonstrate the features of the MPM, one-dimensional wave and impact problems are considered in this section, without employing the viscous damping stress. The simplicity of one-dimensional problems makes it possible to compare the numerical solutions with the analytical solutions available, and to provide a deeper insight into the unique features of the MPM than two- and three-dimensional problems. In Section 4, combined wave and diffusion problems, as observed in recent experiments, are solved by using a two-dimensional MPM code, with the addition of the artificial viscous stress under impact.

Consider an elastic bar with length $L = 1$, Young's modulus $E = 10,000$, and mass density $\rho = 1$ so that the wave speed is $C = \sqrt{E/\rho} = 100$. In the first test problem, a tensile step force $f = 1$ is applied to the bar's right end, with its left end being fixed. Here, we have intentionally defined a problem involving only infinitesimal displacements so that the effects of particle convection and moving boundary can be avoided, which permits a fair comparison between the MPM and FEM solutions. In the MPM simulation, the number of cells is the same as that of particles; in other words, one particle per cell is used. Numerical solutions with different numbers of particles were obtained, which are similar to the finite element solutions with single-point Gauss integration, as shown in Fig. 1 for stress profiles at different times with $N_p = 500$. Essential and natural boundary conditions are enforced at the boundary cell nodes, respectively, while the stress is evaluated at the particles. To investigate whether the code will separate particles when the tensile waves meet in the center, Fig. 2 demonstrates the wave propagation along the same elastic bar, except that both ends are subjected to a step force $f = 1$. By replacing the tensile step force with a compressive rectangular impulse of magnitude 1 and duration L/C , applied at both ends of the bar, Fig. 3a and b illustrate the wave propagation along the elastic bar. Again, the numerical solutions are similar to the finite element solutions. No separation occurs in both tensile and compressive regimes, which is because the existence of at least one particle per cell all the time causes the material to be treated as contiguous and coherent,

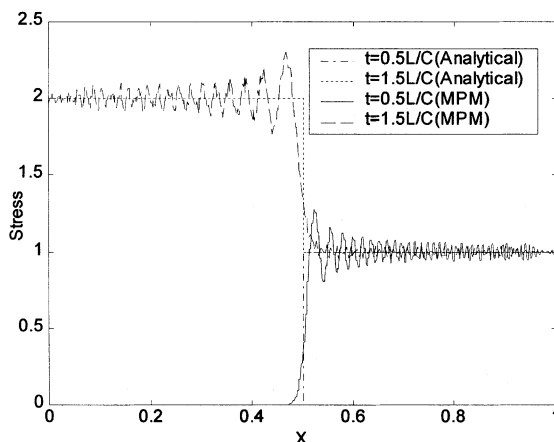


Fig. 1. Stress wave propagation along the bar ($N_p = 500$).

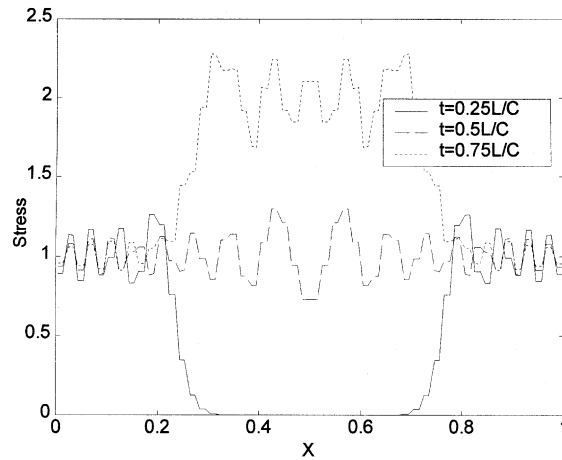


Fig. 2. Elastic stress wave propagation along a bar with both ends subjected to a tensile step force ($N_p = 100$).

namely, no separation. The numerical oscillations can be damped out by employing artificial viscosity, as in the case with the FEM.

Now consider the impact between two elastic bars of equal length $L = 0.5$, with the same material properties as before. The motion of the bars and the corresponding stress wave profiles are shown in Figs. 4 and 5. As can be seen, two bars start to separate from each other when the reflected tensile waves cancel the compressive waves and reach the contact point. To investigate whether a cell without a particle represents a space, elastic wave propagation in two bars separated by an empty cell is illustrated in Figs. 6 and 7. The results appear to be reasonable based on the stress wave profiles in two bars at different times. To examine the impact between two elasto-plastic bars, the motion of the bars and the corresponding stress profiles are given in Figs. 8 and 9, for a linear strain-hardening model with elasto-plastic tangent modulus being a quarter of Young's modulus, and in Figs. 10 and 11, for an elastic-perfect-plastic model. These figures demonstrate the capability of the MPM to simulate wave and impact responses, without invoking master/slave nodes as required in the conventional mesh-based methods such as the FEM.

4. Simulation of combined wave and diffusion responses

Structural failure under external impact loading involves contact, localization, inelasticity, thermal softening, damage evolution, phase transition and fragmentation. The transition from continuous to discontinuous failure modes is characterized by localization, based on the bifurcation analysis of acoustic tensors derived from continuum damage models. As shown in recent analytical and numerical studies [7–9], the onset of localization can be identified via the transition among three basic types of governing differential equations, i.e., hyperbolic (wave), parabolic (thermal diffusion) and elliptic (instantaneous response). Further, the evolution of localization could be represented by a diffusion equation. The formation and propagation of a failure wave in shocked glasses could be considered as a practical and illustrative example [10,11]. It appears that the inelastic deformation can be described as a prompt stress-controlled process that depends only on the local state of material response, if the deformation process can occur in a nearly point-wise manner such as the dislocation motions. However, the evolution of inelastic deformation appears to be a diffusion process if the deformation involves a length scale and can only occur in an essentially random-walk manner. The key issues here are how to identify the physics behind the transition from the stress-wave

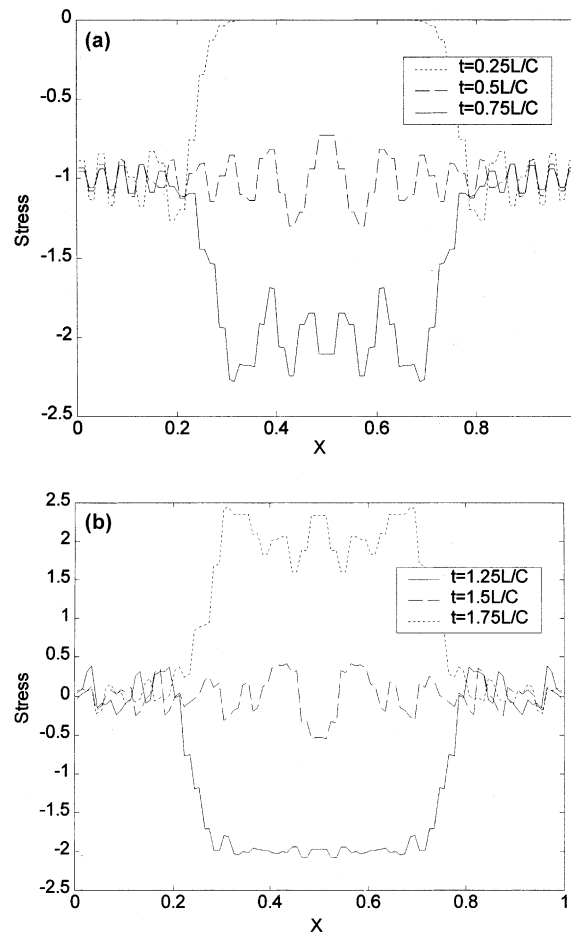


Fig. 3. (a) Elastic stress wave propagation along a bar with both ends subjected to a compressive rectangular impulse force ($N_p = 100$). (b) The continuation of (a).

propagation to a diffusion-controlled process, and how to simulate the dynamic failure processes involving both wave and diffusion in a single computational domain. To resolve these key issues, a combined experimental, analytical and numerical effort is required, which is beyond the scope of the paper.

Based on the previous research results, with the use of the FEM, on combined wave and diffusion modeling for dynamic failure [12] and shock failure [11] without considering the transition from continuous to discontinuous failure modes, an attempt is made in this paper to modify the MPM for combined wave and diffusion problems. The MPM solutions appear to be similar to the FEM solutions with the same constitutive models verified with available experimental data, before the transition from continuous to discontinuous failure modes occurs. However, no master/slave nodes are required if the MPM is used for impact problems. In addition, localized large deformations could be better simulated via the MPM. Based on the framework of the MPM, the transition from continuous to discontinuous failure modes and subsequent cracking could be simulated without changing the mesh connectivity. Hence, it appears that the MPM could become a robust discretization tool to simulate multi-physics problems involving different governing differential equations in a single computational domain.

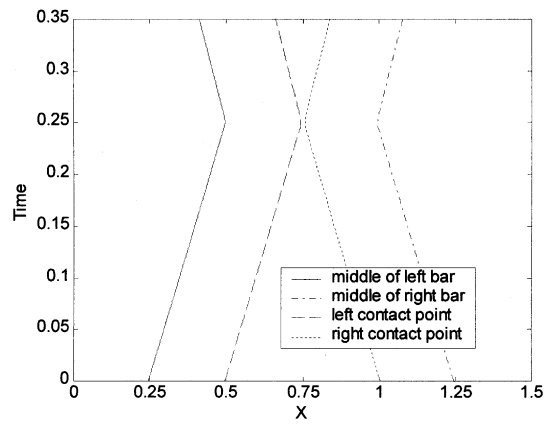


Fig. 4. The impact between two elastic bars ($N_p = 50$ for each bar), the distance between which is 0.5 at $t = 0$. The bars remain in contact for a time of $2L/C$.

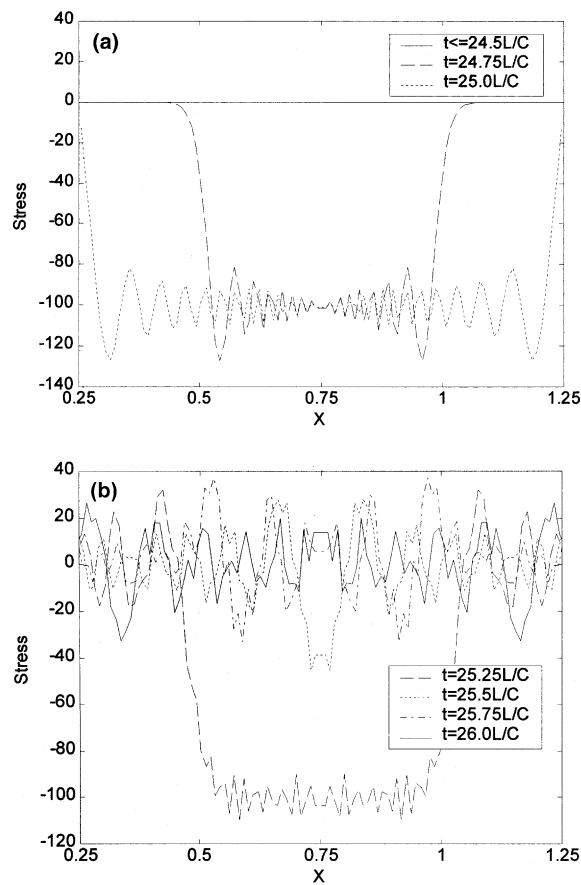


Fig. 5. (a) The changes in the stress profile corresponding to Fig. 4. (b) The continuation of (a).

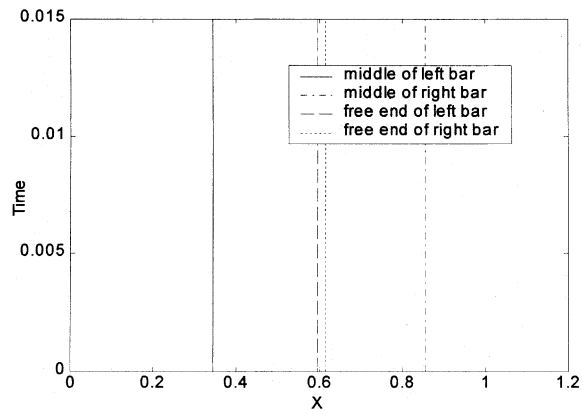


Fig. 6. Elastic wave propagation in two separated bars ($N_p = 50$ for each bar), with the left end of the left bar and the right end of the right bar being subjected to a tensile step force of $f = 1$, respectively.

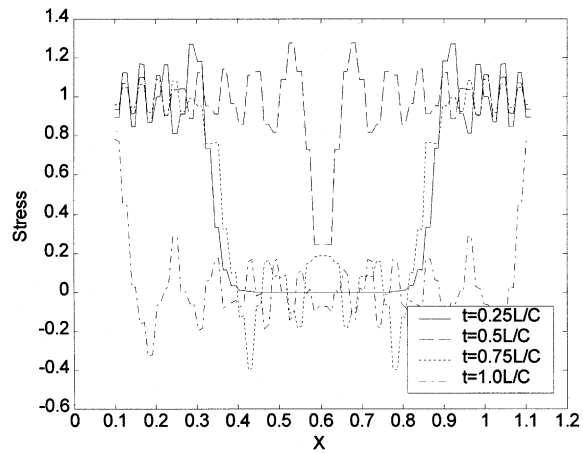


Fig. 7. The stress profile corresponding to Fig. 6.

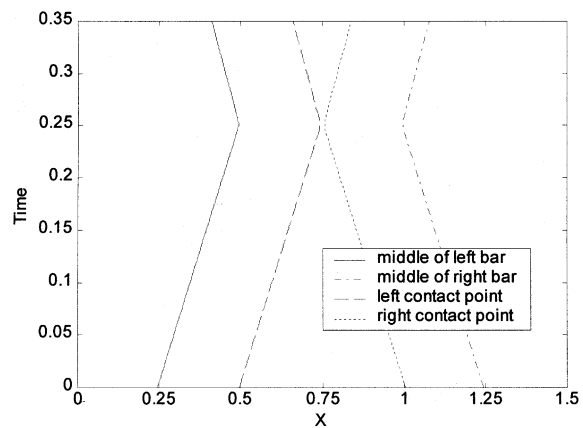


Fig. 8. The impact between two elastic-hardening bars ($N_p = 50$ for each bar), the distance between which is 0.5 at $t = 0$.

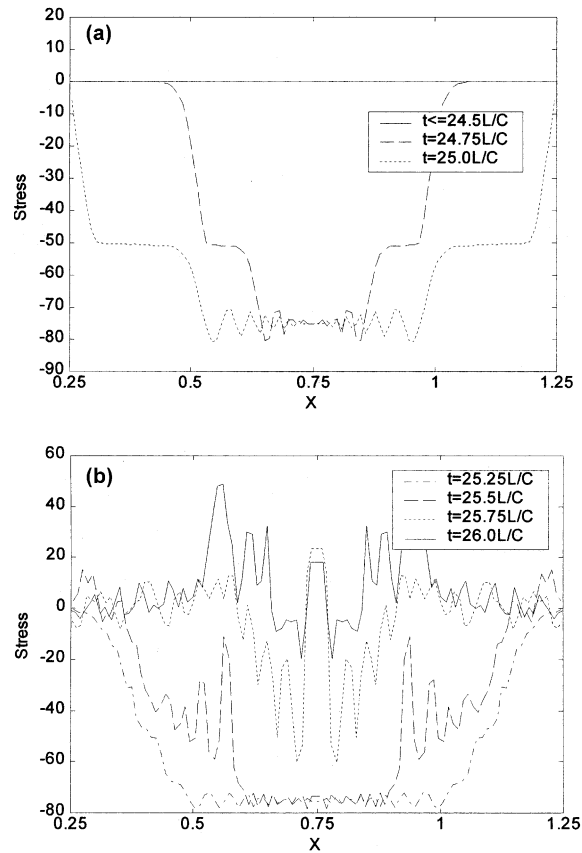


Fig. 9. (a) The changes in the stress profile corresponding to Fig. 8. (b) The continuation of (a).

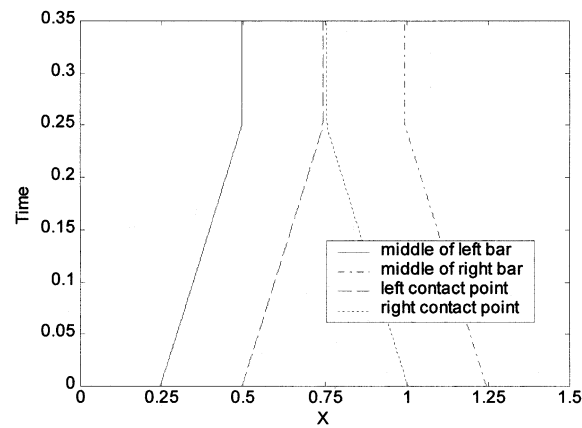


Fig. 10. The impact between two elastic-perfect-plastic bars ($N_p = 50$ for each bar), the distance between which is 0.5 at $t = 0$.

To estimate stress-wave-induced fracturing, a combined damage/plasticity model has evolved over a number of years, which was primarily applied to the case of rock fragmentation as discussed in details by

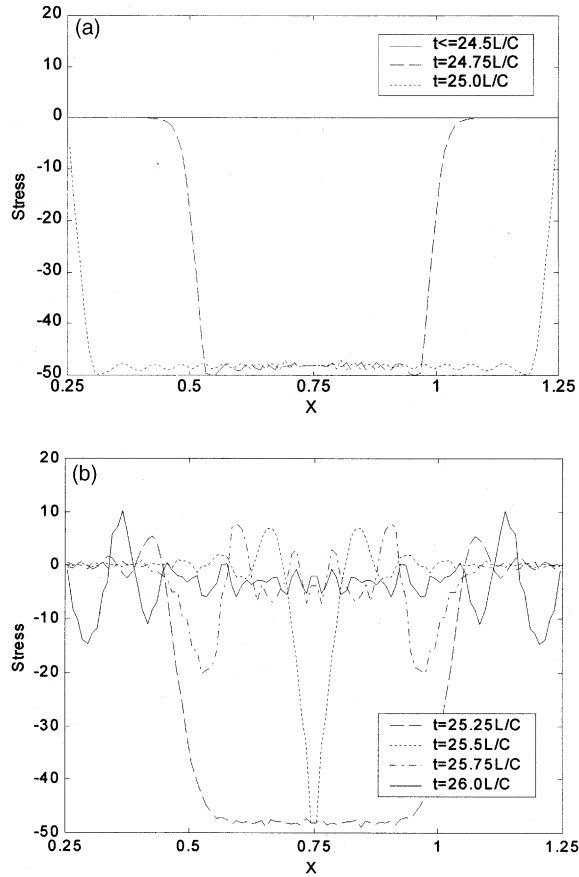


Fig. 11. (a) The changes in the stress profile corresponding to Fig. 10. (b) The continuation of (a).

Chen et al. [12]. Within the loading regime of the model, an isotropic elasticity tensor governs the elastic material behavior; a scalar measure of damage is active through the degradation of the elasticity tensor if the confining pressure $P \geq 0$ (tensile regime); and a pressure-dependent perfectly plastic model is used if $P < 0$ (compressive regime) after a critical state is reached. The evolution equation for tensile damage can be described with the use of the following equations [12]:

$$C_d = \frac{5k}{2} \left(\frac{K_{IC}}{\rho c \dot{\epsilon}_{\max}} \right)^2 \epsilon_v^m \quad (23a)$$

$$D = \frac{16(1 - \bar{\nu}^2)}{9(1 - 2\bar{\nu})} C_d \quad (23b)$$

$$\bar{K} = (1 - D)K \quad (23c)$$

$$\bar{\nu} = \nu(1 - \alpha C_d) \quad (23d)$$

in which C_d is a crack-density parameter, K_{IC} the fracture toughness, ϵ_v the mean volumetric strain, $\dot{\epsilon}_{\max}$ the maximum volumetric strain rate experienced by the material at fracture, c the uniaxial wave speed

$\sqrt{E/\rho}$ with E being Young's modulus, and D a single damage parameter. Also, K and ν are the original bulk modulus and Poisson's ratio, respectively, for the undamaged material, and the barred quantities represent the corresponding parameters of the damaged material. The model parameters k and m can be determined by using the fracture stress versus strain rate curve. The unloading/reloading moduli are obtained by choosing $\alpha = 16\beta/9$ with β being the fraction of damage.

To simulate the dynamic failure evolution of a class of brittle solids, a strain-based damage diffusion equation is combined with the above tensile damage model. As a result, mesh-independent solutions can be obtained without invoking nonlocal or gradient models in the strain–stress space, and an efficient numerical scheme can be designed for parallel-computer simulation of structural failure. If the bifurcation analysis identifies the onset of localization, a surface of discontinuity will be driven by the heterogeneity and stress concentration, with \mathbf{n} being the vector normal to the surface. The law of damage diffusion is assumed to be

$$\mathbf{J} = -d \frac{\partial C}{\partial \mathbf{n}} \quad (24)$$

where C is the concentration of microcracks, \mathbf{J} the flux of microcracks, and d a damage diffusivity function. If the damage diffusion is assumed to be isotropic, a damage diffusivity function of mode I at any location \mathbf{x} and time t can be defined to be

$$d(\mathbf{x}, t) = \lambda_1 \frac{\varepsilon_{vf} - \varepsilon_v}{\varepsilon_{vf}} \quad (25)$$

in which ε_{vf} represents the value of ε_v at the final state before rupture. As can be seen from Eq. (25), the diffusion process will diminish with the evolution of microcracking and the model parameter λ_1 controls the rate of diffusion. To initiate the diffusion of damage at the imperfection point, an internal damage evolution per unit time is given by

$$Q(\mathbf{x}, t) = \frac{5k}{2T_d} \left(\frac{K_{IC}}{\rho c \dot{\varepsilon}_{\max}} \right)^2 \varepsilon_v^m \quad (26)$$

if $\varepsilon_v - \varepsilon_{v1} \geq 0$, based on Eq. (23a) that is local. In Eq. (26), T_d and ε_{v1} denote the characteristic time of the concentration diffusion of microcracks and the critical state strain, respectively. The concentration of microcracks C is related to the crack-density parameter C_d that represents the volume fraction of material made up of microcracks, namely

$$C_d = \lambda_2 C \quad (27)$$

where λ_2 is the characteristic volume of a microcrack. Based on the previous research results [11,12], the equation governing the tensile damage diffusion can then be written as

$$\frac{\partial C}{\partial t} = \frac{\partial}{\partial \mathbf{n}} \cdot \left(d \frac{\partial C}{\partial \mathbf{n}} \right) + Q \quad (28)$$

The above diffusion equation can be solved in parallel with the wave equation to simulate the evolution of localization. For each time step, the strain field obtained from the wave equation will be the input to the diffusion equation, and the concentration of microcracks found from the diffusion equations will be used to calculate the current damage in the strain–stress relation if the critical state is reached. In the parallel (staggered) setting, the time step that satisfies the stability conditions of forward time integrators used in both wave and diffusion equation solvers is employed to solve the whole problem at the same time.

To demonstrate the proposed procedure, consider a plane problem as shown in Fig. 12. The dimensions used are $L_x = 1.0$ m and $L_y = 1.5$ m. The initial conditions consist of zero displacement and zero velocity

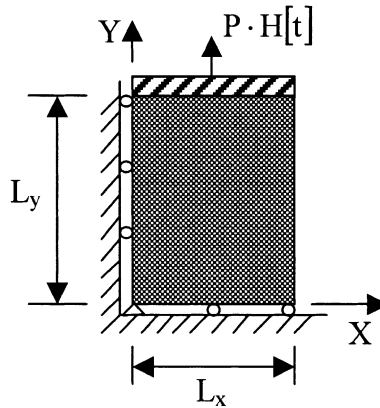


Fig. 12. The problem geometry and boundary conditions for two-dimensional simulation.

throughout the problem domain, while the boundary condition is shown in Fig. 12. A constant load is suddenly applied through a mechanism that provides no lateral constraint and ensures that the displacement in the y -direction is the same for all points on the upper surface. To permit a fair comparison between the MPM and FEM solutions, only infinitesimal displacements are considered so that the effects of particle convection and moving boundary can be avoided. Three finite element meshes are used, with Mesh I, II and III being defined to be 10×15 , 16×24 and 20×30 quadrilateral cells with each cell consisting of four triangle constant stress elements, respectively. Thus, three MPM meshes can be designed with each cell consisting of four material points, corresponding to the finite element meshes. The boundary conditions are enforced on the cell nodes to solve Eq. (18). The central-difference in space is adopted to discretize Eq. (28), based on the cell nodes. The concentration of microcracks in a cell, which is calculated from the diffusion equation, is evenly distributed to the triangle elements or material points contained in the cell. The strain value averaged over the triangle elements or material points in a cell is used in the diffusion equation. With the assumption that the origin is a weak spot, a circular damage contour will evolve from the origin, with \mathbf{n} being the vector normal to the contour. The model parameters are assigned the following values:

$$E = 50 \text{ GPa}, \quad \nu = 0.3, \quad \rho = 2500 \text{ kg/m}^3, \quad K_{IC} = 1.0 \text{ MPa}\sqrt{\text{m}}, \quad m = 7, \quad k = 5 \times 10^{22} \text{ m}^{-3}, \\ \varepsilon_{vl} = 0.002, \quad \varepsilon_{vf} = 0.01, \quad T_d = 0.01, \quad \lambda_1 = 500, \quad \lambda_2 = 0.01$$

which are representative of geologic materials. As shown in Figs. 13–15, the damage contour is converged with the mesh refinement, and both the FEM and MPM yield the similar results.

To further demonstrate the proposed procedure, the failure wave problem as observed in shocked glasses is considered here, based on the previous work [10,11]. It has been observed in plate impact experiments that some brittle solids may undergo elastic deformation at the shock wavefront, and fail catastrophically at a later time when they are shocked near but below the apparent Hugoniot elastic limit. Because this phenomenon appears to have features different from those of usual inelastic waves, it has been interpreted as the failure wave. It has been proposed that the progressive percolation of microfissures from the impact surface into the material bulk give rise to the observed failure wave phenomenon. To provide a general framework for modeling such a dynamic material response, a three-dimensional continuum damage model has been recently developed [11], where the progressive microdamage percolation lagging behind the elastic shock wave is described by a nonlinear diffusion equation throughout the continuum body. Macroscopic

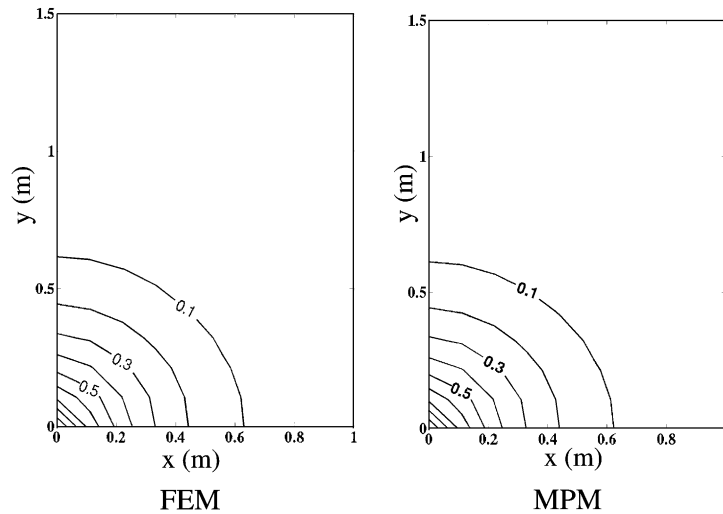


Fig. 13. Comparison between the damage contours simulated by the FEM and MPM, with the use of Mesh I.

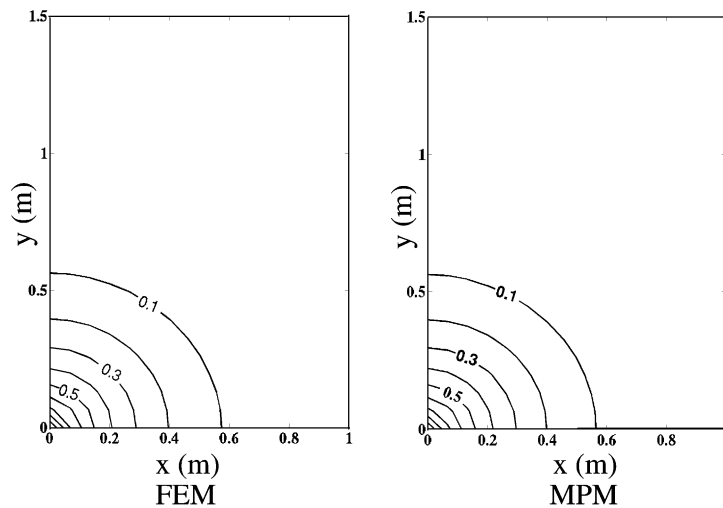


Fig. 14. Comparison between the damage contours simulated by the FEM and MPM, with the use of Mesh II.

shear-induced dilatancy is assumed and treated as a one-to-one measure of the mean intensity of micro-damage. The damage-driven stress state evolution is determined based on the assumption that the deviatoric strain energy in the elastically compressed material (undamaged) is converted, through the damaging process, into the volumetric potential energy in the comminuted and dilated material. The diffusion equation governing microdamage evolution and the wave equation governing elastic shock compression have been solved via a staggered manner with the use of the FEM and FDM [11]. In this paper, the MPM is used to discretize the wave equation in space. As a result, the target and flyer can be separated from each other before impact occurs. If the FEM is used, the target and flyer must be bonded together, with the flyer

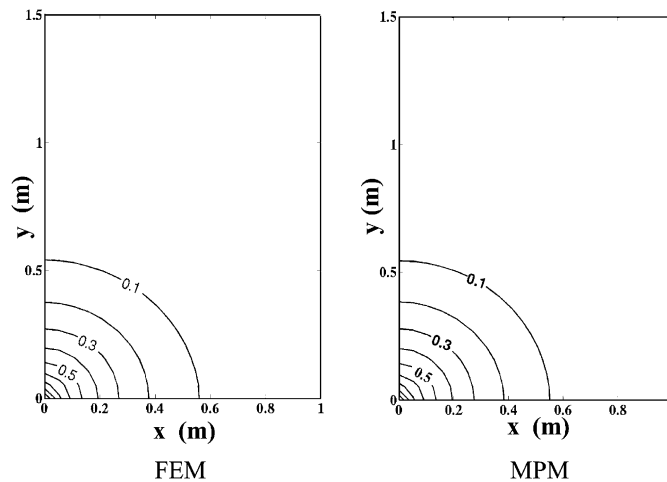


Fig. 15. Comparison between the damage contours simulated by the FEM and MPM, with the use of Mesh III.

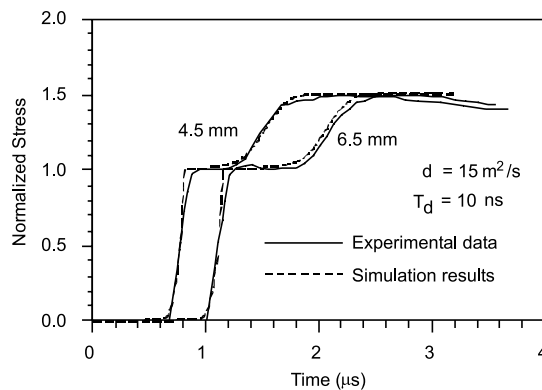


Fig. 16. Comparison of the model prediction with experimental data.

being given a constant velocity at the beginning of simulation, to avoid the use of master/slave nodes when impact occurs. After the flyer impacts the target in the MPM simulation, the central-difference in space is adopted to discretize the diffusion equation, based on the cell nodes. In the staggered setting, the time step satisfying the stability conditions of forward time integrators used in both wave and diffusion equation solvers is employed to solve the whole problem at the same time. With the use of the same model parameters and problem geometry as used in the previous work [11], Fig. 16 illustrates the comparison of the model predictions with experimental data for the material point located at 4.5 and 6.5 mm away from the impact surface, respectively. The corresponding longitudinal and lateral stresses predicted by the model are shown in Fig. 17. Both the FEM (four triangle elements in each quadrilateral cell) and MPM (four material points in each quadrilateral cell) yield the similar solutions, and are converged with the mesh refinement. A sharp wavefront can be produced with a very small amount of viscous damping if the wave equation is combined with a diffusion equation in both the FEM and MPM calculations, as compared with pure wave problems.

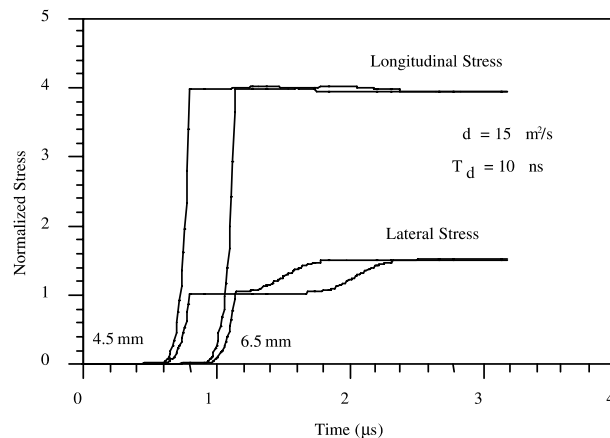


Fig. 17. The longitudinal and lateral stresses of model prediction corresponding to Fig. 16.

5. Concluding remarks and discussions

To evaluate the potential of the MPM in simulating dynamic brittle failure involving different failure modes, the essential features of the MPM have been explored for wave and impact problems, and combined wave and diffusion problems in this paper. Through the comparison with the experimental, analytical and numerical data available, it appears that the MPM, as one of the newly developed spatial discretization methods, is a robust tool to simulate multi-physics problems such as dynamic brittle failure under impact.

As indicated by Belytschko et al. [13], the “meshless (meshfree)” methods are uniquely suitable for those problems, for which the conventional mesh-based methods are awkward, such as localized large deformations, propagation of cracks, and separation of continuum. In fact, the key difference among different spatial discretization methods is how the gradient and divergence terms are calculated. Because the meshless methods do not use a rigid mesh connectivity as compared with the FEM, FDM and BEM, the interpolation in the moving domain of influence is the common feature of the meshless methods. Although a background mesh is used to calculate the gradient and divergence terms, the MPM is still based on the interpolation in the moving domain of influence, namely, the spatial discretization is continuously adjusted as a body deforms. Thus, the MPM can be considered as one of the meshless methods. To our knowledge, all existing meshless methods employ some sort of moving domain of influence to find the gradient and divergence terms. Hence, the word “meshless” should be interpreted as meaning that a rigid mesh connectivity is not used in spatial discretization.

With the use of different approaches to calculate gradient and divergence terms, different meshless methods have demonstrated the robustness and potential in different types of problems. Based on the literature survey, however, it appears that the MPM is particularly well suited to penetration and perforation problems, and could be easily implemented into existing production FEM codes due to its strong connection to the FEM, as compared with other meshless methods. Future research will aim at taking advantages of different spatial discretization methods, including both mesh-based and meshfree ones, to better simulate those complex problems such as impact/contact, localization, crack propagation, penetration, perforation, fragmentation, and interactions among different material phases, in a unified computational framework. A combined experimental, analytical and computational effort is required to further validate and verify the proposed simulation tool before it can be used, with confidence, for general applications.

Acknowledgements

This research was sponsored in part by the National Science Foundation with Dr. K. Chong being program director. Part of this work was performed at Sandia National Laboratories. Sandia is a multi-program laboratory operated by Sandia Corporation, a Lockheed Martin Company, for the United States Department of Energy under Contract DE-ALO4-04AL8500. The authors are grateful to the reviewers for discerning comments on this paper.

References

- [1] Harlow FH. The particle-in-cell computing method for fluid dynamics in fundamental methods in hydrodynamics. In: Alder B, Fernbach S, Rotenberg M, editors. *Experimental arithmetic, high-speed computations and mathematics*. New York: Academic Press; 1964. p. 319–45.
- [2] Sulsky D, Chen Z, Schreyer HL. A particle method for history-dependent materials. *Comput Meth Appl Mech Eng* 1994;118:179–96.
- [3] Sulsky D, Zhou SJ, Schreyer HL. Application of a particle-in-cell method to solid mechanics. *Comput Phys Commun* 1995;87:236–52.
- [4] Sulsky D, Schreyer HL. Axisymmetric form of the material point method with applications to upsetting and Taylor impact problems. *Comput Meth Appl Mech Eng* 1996;139:409–29.
- [5] York AR II, Sulsky D, Schreyer HL. Fluid–membrane interaction based on the material point method. *Int J Numer Meth Eng* 2000;48(6):901–24.
- [6] Wilkins ML. Use of artificial viscosity in multidimensional fluid dynamic calculations. *J Comput Phys* 1980;36:281–303.
- [7] Chen Z, Xin X, Qian D. A study of localization problems based on the transition between governing equations. *Int J Adv Struct Eng* 1998;2(4):291–306.
- [8] Xin X, Chen Z. An analytical solution with local elastoplastic models for the evolution of dynamic softening. *Int J Solid Struct* 2000;37:5855–72.
- [9] Xin X, Chen Z. An analytical and numerical study to simulate the evolution of dynamic failure with local elastodamage models. *Int J Damage Mech* 2000;9(4):305–28.
- [10] Chen Z, Xin X. An analytical and numerical study of failure waves. *Int J Solid Struct* 1999;36:3977–91.
- [11] Chen Z, Feng R, Xin X, Shen L. A computational model for impact failure with shear-induced dilatancy. *Int J Numer Meth Eng*, accepted for publication.
- [12] Chen Z, Hu W, Chen EP. Simulation of dynamic failure evolution in brittle solids without using nonlocal terms in the strain–stress space. *Comput Model Eng Sci* 2000;1(4):101–6.
- [13] Belytschko T, Krongauz Y, Organ D, Fleming M, Krysl P. Meshless methods: An overview and recent developments. *Comput Meth Appl Mech Eng* 1996;139:3–48.